# Validation of the Numerical Simulation of Rotor/stator Interactions in Aircraft Engine Low-Pressure Compressors

Isabelle Favretti, Louis Roux, Alain Batailly

## To cite this version:

Isabelle Favretti, Louis Roux, Alain Batailly. Validation of the Numerical Simulation of Rotor/stator Interactions in Aircraft Engine Low-Pressure Compressors. Journal of Engineering for Gas Turbines and Power, 2025, 147 (5), ⟨10.1115/1.4066789⟩. ⟨hal-04871166⟩

HAL Id: hal-04871166
https://hal.science/hal-04871166v1

Submitted on 7 Jan 2025

POLYTECHNIQUE MONTRÉAL
UNIVERSITÉ D'INGÉNIERIE

LABORATOIRE D'ANALYSE VIBRATOIRE ET ACOUSTIQUE

# Validation of the Numerical Simulation of Rotor/stator Interactions in Aircraft Engine Low-Pressure Compressors

I. Favretti[1], L. Roux[2], A. Batailly[1]

**Abstract**

This contribution focuses on the validation of a numerical strategy developed jointly by Safran and Polytechnique Montréal for the simulation and the analysis of blade-tip/casing contact interactions in low-pressure compressor stages. A large experimental campaign provided data (including strain measurements on the blade and abradable coating wear profiles) for several contact configurations involving four distinct blades and one type of abradable coating. The numerical strategy is here improved by introducing a new cut-off criterion to ensure the physical relevance of the presented results, specifically by keeping the maximum stress within the blade below the material's yield stress. Similarly to previous publications involving a single contact configuration, the numerical model is first calibrated for one of the four blades of interest. It is seen that the results using the numerical model—critical speed, relative wear depth between leading edge and trailing edge, maximum stress levels within the blade—are in good agreement with the experimental observations. Using the same calibration, numerical simulations are then blindly run for the three other blades. The results demonstrate that numerically predicted key quantities align well with experimental data. Additionally, the numerical model provides an accurate relative assessment of a blade's sensitivity to contact in agreement with experimental observations. This paper thus presents the first blind validation of a numerical strategy dedicated to blade-tip/casing contact interactions. Simultaneously, it also demonstrates that this model may be considered for the early discrimination of blade profiles depending on their sensitivity to contact.

**Keywords**

Rotor/stator interactions, blade tip/casing contacts, abradable coating, test bench, numerical simulations

1 - Département de génie mécanique, École Polytechnique de Montréal, P.O. Box 6079, Succ. Centre-Ville, Montréal, Québec, Canada H3C 3A7
2 - Safran Aero Boosters, Liège, Belgique

# Validation de la simulation numérique d'interactions rotor/stator dans des compresseurs basse pression de moteurs d'avion

I. Favretti[1], L. Roux[2], A. Batailly[1]

**Résumé**

Cet article porte sur la validation d'une stratégie numérique développée conjointement par Safran et Polytechnique Montréal pour la simulation et l'analyse d'interactions de contact aube/carter dans les compresseurs basse pression de moteurs d'avion. Une campagne expérimentale de grande ampleur a permis d'obtenir des données de référence (incluant des mesures par jauges de contraintes et l'usure de revêtements abradables) pour plusieurs configurations de contact impliquant quatre aubes distinctes et un type de revêtement abradable. La stratégie numérique est également enrichie grâce à l'introduction d'un critère fusible permettant d'assurer la pertinence physique des résultats obtenus, en vérifiant que la contrainte maximale dans l'aube en contact ne dépasse pas sa limite d'élasticité. Le modèle numérique est calibré en ne considérant qu'une seule des quatre configurations de contact avec une seule aube. Les résultats obtenus démontrent un excellent accord en termes de vitesse critique, d'usures relatives du revêtement abradable et de contraintes maximales dans l'aube avec les valeurs obtenues expérimentalement. Sur base de cette calibration, les autres configurations de contact avec les autres aubes sont ensuite simulées en aveugle, sans calibration additionnelle. Les résultats obtenus démontrent que les valeurs prédites numériquement sont cohérentes avec les observations expérimentales. Cet article présente ainsi la première validation en aveugle d'une stratégie numérique dédiée aux interactions de contact aube/carter. De plus, les résultats obtenus soulignent la pertinence d'utiliser une telle stratégie pour la discrimination des profils d'aubes *a priori*, lors des premières phases de conception, en fonction de leur sensibilité au contact.

**Mots-clés**

Interactions rotor/stator, contacts aube/carter, revêtement abradable, banc d'essais, simulation numérique

1 - Département de génie mécanique, École Polytechnique de Montréal, P.O. Box 6079, Succ. Centre-Ville, Montréal, Québec, Canada H3C 3A7
2 - Safran Aero Boosters, Liège, Belgique

## 1 Introduction

Structural contact interactions between blades and their surrounding casing can lead to failure scenarios within aircraft engines' compressor or turbine stages [1]. Today, the occurrence of such rotor/stator interactions is increasingly likely as the drive towards more efficient and greener engines calls for reduced tip clearances. These interactions are intrinsically multiphysics [2], featuring very high relative speeds, and involve very sophisticated wear phenomena of the abradable coating often deposited on the casing [3]. Their complexity has driven researchers to adopt a two-pronged approach relying on simplified experimental setups and advanced numerical models to try to better understand and predict them.

From an experimental standpoint, several setups have been designed to analyze blade/abradable coating interactions, which are also referred to as rubbing interactions. While the focus was initially placed on the characterization of the abradable coating material properties [4], researchers also took an early interest in analyzing the blade's dynamics [5, 6]. More recently, experimental setups have been designed with advanced instrumentation in order to better understand intricate wear phenomena of the abradable coating [7] including grooving phenomena, casing-to-blade material transfer [5] and even rotor-to-casing material transfer [8]. Nonetheless, most of the aforementioned experimental setups involve simplified blade designs such as a thin beam or even a very small and stiff mock blade. The costs associated with the development of full-scale experimental setups and potential confidentiality issues led to a very scarce number of publications involving actual aircraft engine blades. To date, only a few publications are available on the subject [9, 10]. To the best of the authors' knowledge, this recent experimental campaign [11] is the most comprehensive, since it involves several blade geometries interacting with one abradable material.

From a numerical standpoint, the simulation of blade-tip/casing contacts is challenging as it involves complex mechanical models impacting each other with very high relative speeds. Initially involving analytical [12] or simplified [13] mechanical models, the simulation models progressively evolved towards the inclusion of full 3D finite element models [14], abradable coating wear [15, 16], thermomechanics [17], mistuning [18] and geometric nonlinearities [19]. The transient nature of the phenomena witnessed on full-scale experimental setups initially motivated researchers to rely on time integration-based strategies [20], but frequency domain-based strategies have also been proposed [21].

From a general point of view, in simulation based engineering science, numerical models must be thoroughly verified and validated. With respect to the verification of numerical methodologies employed for the simulation of blade-tip/casing contacts, recent studies have demonstrated that time integration-based and frequency domain-based numerical strategies lead to consistent results [21]. Numerical cross-verification has proven to be essential to discriminate numerical artefacts from what may be assumed physically relevant results. In addition, the complementarity of both types of methodologies was also underlined [22]. The validation of numerical strategies dedicated to blade-tip/casing contact interactions has, so far, mostly been based on limited experimental data involving only one blade type [23]. As a consequence, while it was possible to assess the accuracy of a given numerical strategy for a given contact scenario [9], it has not yet been possible to assess its versatility should a mechanical component of the experimental setups be modified (blade or abradable coating for instance). As of today, a few publications have demonstrated the validation of time integration-based strategies on full-scale experimental setups for a single blade [24].

This article presents the validation of an in-house numerical tool for the prediction of blade-tip/casing contact interactions [25] based on experimental results shared by the industrial partner. Section 2 introduces the experimental setup and its key characteristics. The instrumentation of the setup and the different contact scenarios that are considered are also presented in details. In section 3, the results obtained from one of the contact scenario, which has been arbitrarily considered as a reference contact scenario for the sake of numerical calibration, are discussed. The numerical calibration of the time integration-based numerical strategy, hereafter referred to as Coros (COntact ROtor/Stator), on this reference contact scenario is detailed in section 4. Section 5 addresses the determination of the cut-off criterion. Results obtained from blind numerical simulations carried out on the other contact scenarios are given in section 6.

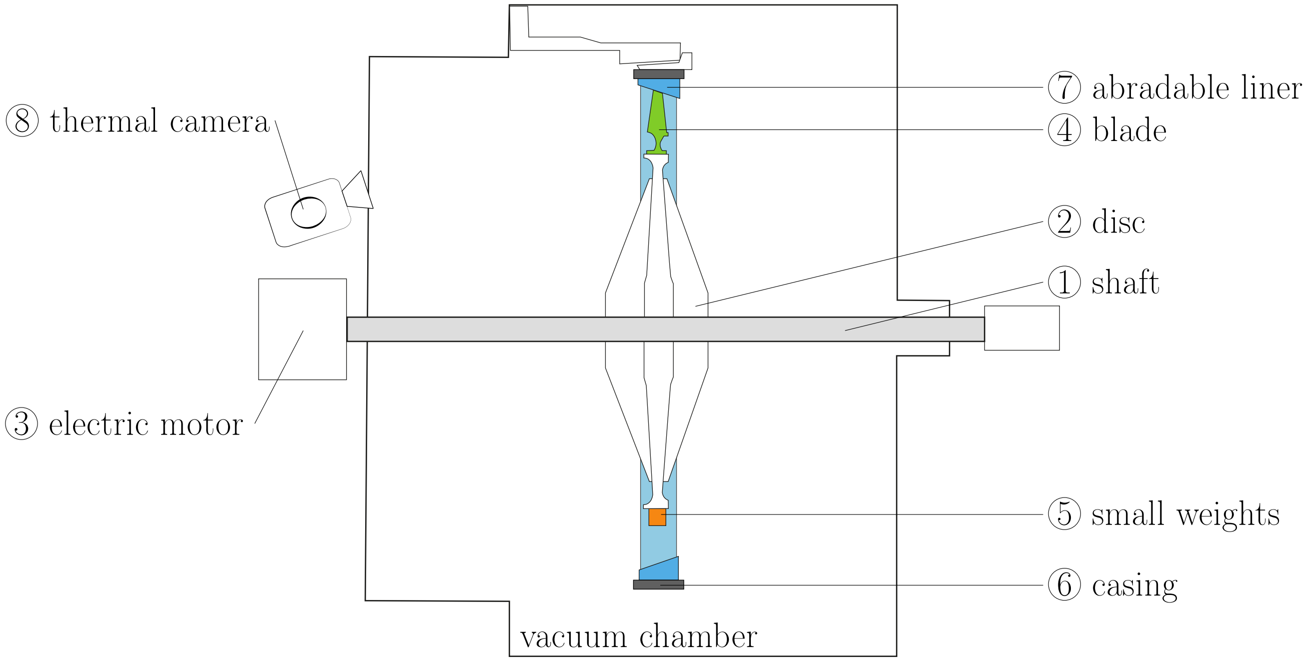

**Figure 1.** Experimental setup.

## 2 Experimental setup

A full scale test rig has been designed to investigate rotor/stator interactions within a compressor stage as shown in Fig. 1. Details about this experimental setup have already been published [11], thus only key aspects of it are mentioned here for sake of completeness. The test bench consists of a full rotor disc, which is mounted with a single blade and balanced using small weights. Precise shaft alignment with respect to the casing is carefully executed. An AlSi-Po-based abradable is sprayed onto the casing contact surface and aligned axially with the blade. The blade is attached to the disc with a custom mount allowing for mechanical characteristics similar to the conventional firtree assembly. Tests are conducted at ambient temperature, and the entire rig is placed in a vacuum chamber so that aerodynamic forcing is considered negligible. In total, four different blades—namely B1, B2, B3 and B4—are considered. The blade-tip/casing contact interaction experimentally simulated with the blade B1 has been arbitrarily chosen as a calibration point and will be referred to as the *calibration test* in the remainder.

### 2.1 Testing procedure

Contact between the rotating blade and the abradable coating is initiated by the application of centrifugal effects as the blade angular speed increases. In order to achieve contact at a given angular speed, tip clearances at rest are finely tuned using clearance captors and axial shims. If the target angular speed is reached before contact is established, the test is interrupted and the radial clearances are readjusted. Once the blade begins to rub, the angular speed of the rotor is maintained constant throughout the duration of the interaction.

### 2.2 Instrumentation

Interactions are monitored using multiple instruments. Strain gauges located on the main components of the test bench—casing, disc and blade—record their dynamic responses. In addition, an infrared camera points toward a glassed section of the bench, offering a view on the blade-tip/casing interface. This allows the estimation of temperature rise at the contact areas. Tip clearance sensors are also used to prepare the bench before each test.

## 3 Calibration test

This section presents the experimental data collected during the test performed on the reference blade B1.

### 3.1 Blade of interest

Blade B1, made of a titanium alloy, belongs to the fourth stage of a low-pressure compressor. On the test bench, it is instrumented with four strain gauges (G1 to G4), see Fig. 2.

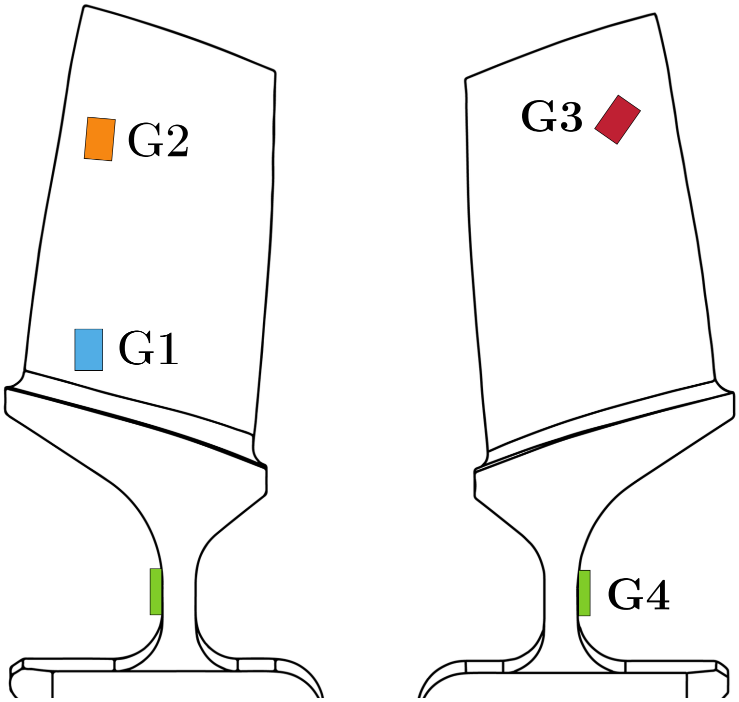

**(a)** Suction side. **(b)** Pressure side.

**Figure 2.** Strain gauges on blade B1.

### 3.2 Contact scenario

Based on the blade's modal properties and empirical observations related to its dynamic response when subjected to contact, engineers were able to determine a potential critical angular speed. Such identification is arduous as the estimation of contact stiffening—meaning the increase of the blade's first eigenfrequencies during contact interactions—cannot be theoretically predicted. Hence, a Campbell diagram alone is not sufficient to determine the potential critical speed; a trial and error-based approach is oftentimes needed. Accounting for centrifugal effects, tip clearances at rest are tuned so that blade-tip/abradable coating contacts occur at the predicted critical angular speed.

### 3.3 Hardware observations

As per Fig. 3, significant damage is noticed on B1 in two different locations. Cracks, some more than one centimeter long, are visible along the blade root fillet at the leading edge (LE). The tip of the blade is also damaged due to repetitive contacts with the casing. The abradable liner shows eight wear lobes equally distributed along its circumference. This wear pattern is indicative of an interaction with the $8^{th}$ engine order (EO). Post-test CMM analyses confirm an 8-lobed pattern in front of the TE and the middle of chord (see Fig. 4). No clear pattern can be observed at the leading edge (4a). At the middle of the chord, the maximum wear depth reaches 0.681 mm, contrasting with some areas of the abradable material that remain untouched (see $\theta = 270°$).

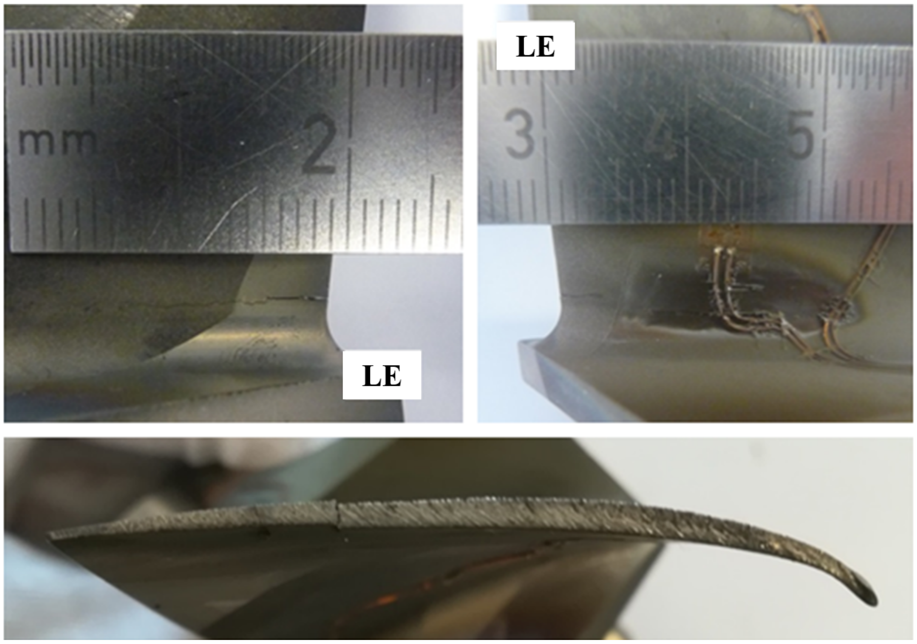

**Figure 3.** Damage on blade B1 [11].

### 3.4 Strain gauge signals

Strain gauges favorably provide insight on the chronology of the interaction. Time signals acquired from the four strain gauges (G1 to G4) attached to B1 are presented in Fig. 5 over a time interval of 30 seconds. Following the initial contact occurring around $t = 18$ s, amplitudes of vibration consistently increase over time. Sensitive to bending mode 1B, G1 exhibits the highest amplitudes to a point where it becomes saturated ($t = 36$s). Absolute amplitudes for G1 are then disregarded from this instant onward. Amplitudes of gauge G4, associated to the edgewise mode, are also increasing, but remain low compared to other gauges. G2 and G3, respectively sensitive to modes 2B and 1T, demonstrate their participation in the interaction in a lesser proportion than G1. These signals thus indicate that the blade cracked at its foot under excessive bending stress. Strain gauge G1 is chosen to study the blade's dynamics during the test since it is the gauge most sensitive to mode 1B involved in the interaction. The strain signal can be divided in four distinct phases identified in Fig. 5, from the beginning of the test (phase 0 at $t = 0$s), to the loss of contact between the blade and the abradable at $t = 39$ s (end of phase 3). To distinguish these phases, the variation of the signal's frequency content is visualised using a spectrogram obtained with a short-time Fourier transform. The intensity of the color scales with the magnitude of the signal. Engine orders and natural frequencies of B1 are added on the y-axis. The spectrogram shows that during phase 2, the blade's frequency is becoming synchronized with the EO8 as it undergoes contact stiffening. The synchronization is observed at a frequency 11% higher than its predicted natural frequency at $\Omega_c$. The percentage of contact stiffening is obtained from the ratio between the predicted natural frequency, read off a Campbell diagram, and the actual interaction frequency.

To better understand the interaction, each phase is detailed and illustrated using polar representations of the time signals. This facilitates the identification of vibration patterns.

**Phase 0 - Before contact** : $t \in [0; 13.5]$s, see Fig. 7a, the rotor accelerates to the target speed, and the blade vibrates at its natural frequencies.

**Phase 1 - First touch** : $t \in [13.5; 17.6]$s, see Fig. 7b, the frequency content becomes richer after the initial contact. Amplitudes remain low at this stage.

**Phase 2 - Contact stiffening** : $t \in [17.6; 22.7]$s, see Fig. 7c and 7d, the blade's own modes stiffen due to contact. Mode 1B shifts between EO7 (phase 2a) and EO8 (phase 2b) as its frequency increases. Both modes 1B and 1T participate in the interaction.

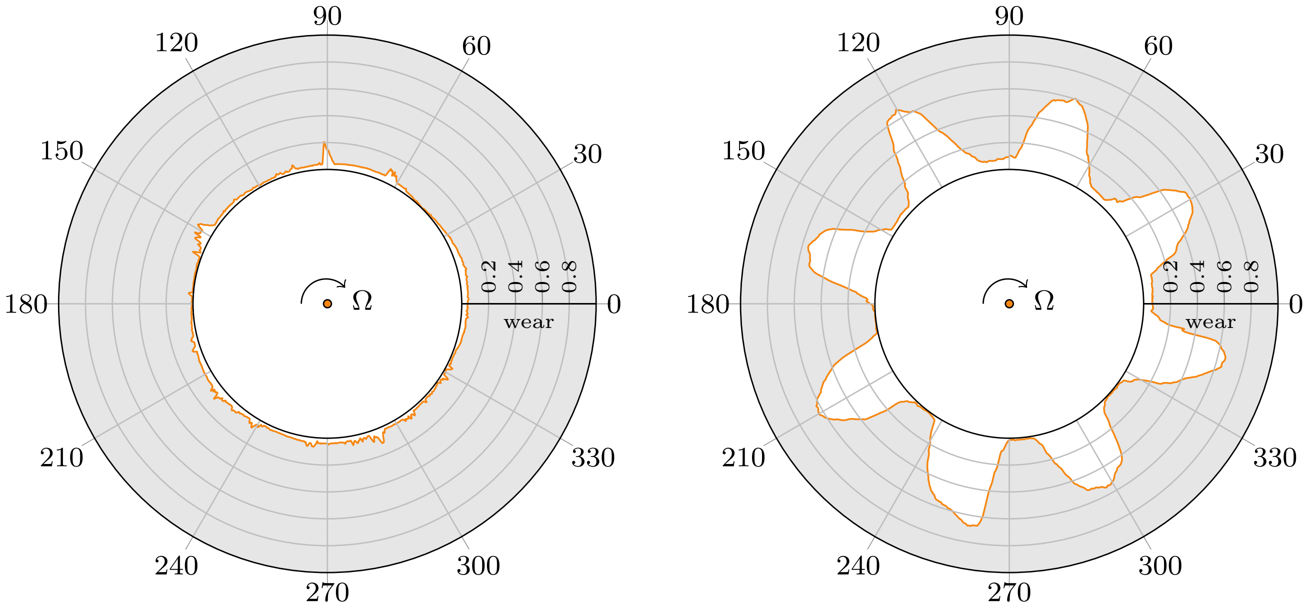

**(a)** LE

**(b)** Mid Chord

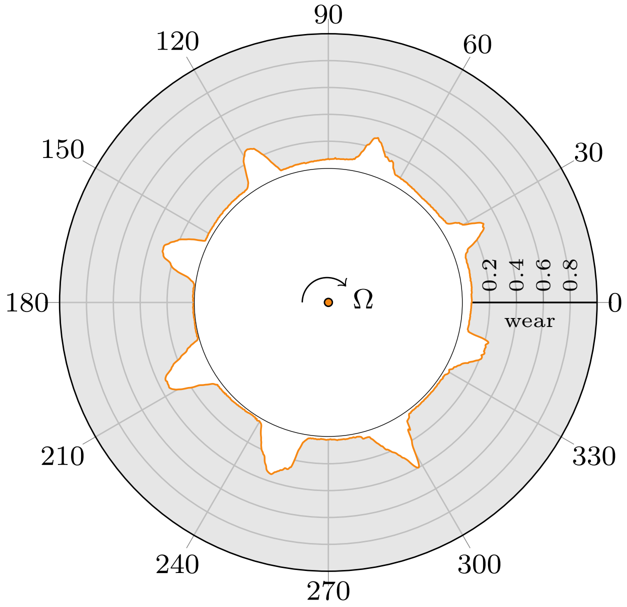

**(c)** TE

**Figure 4.** Wear profiles after the reference test on B1.

**Phase 3 - Synchronized interaction** : $t \in [22.7; 39]$s, see Fig. 7e, the first bending mode achieves perfect synchronization with EO8, resulting in exactly eight oscillations of the blade per revolution. Strain levels increase until G1's saturation and, ultimately, blade rupture.

Figures 6b and 7d offer a good visualisation of the contact stiffening phenomenon. The latter is responsible of the variation of the frequency of mode 1B, which is represented as the wavelike pattern on the spectrogram, as well as the superimposition patterns with 7 or 8 lobes. Participation of mode 1T with EO21 (multiple of 7) contributes

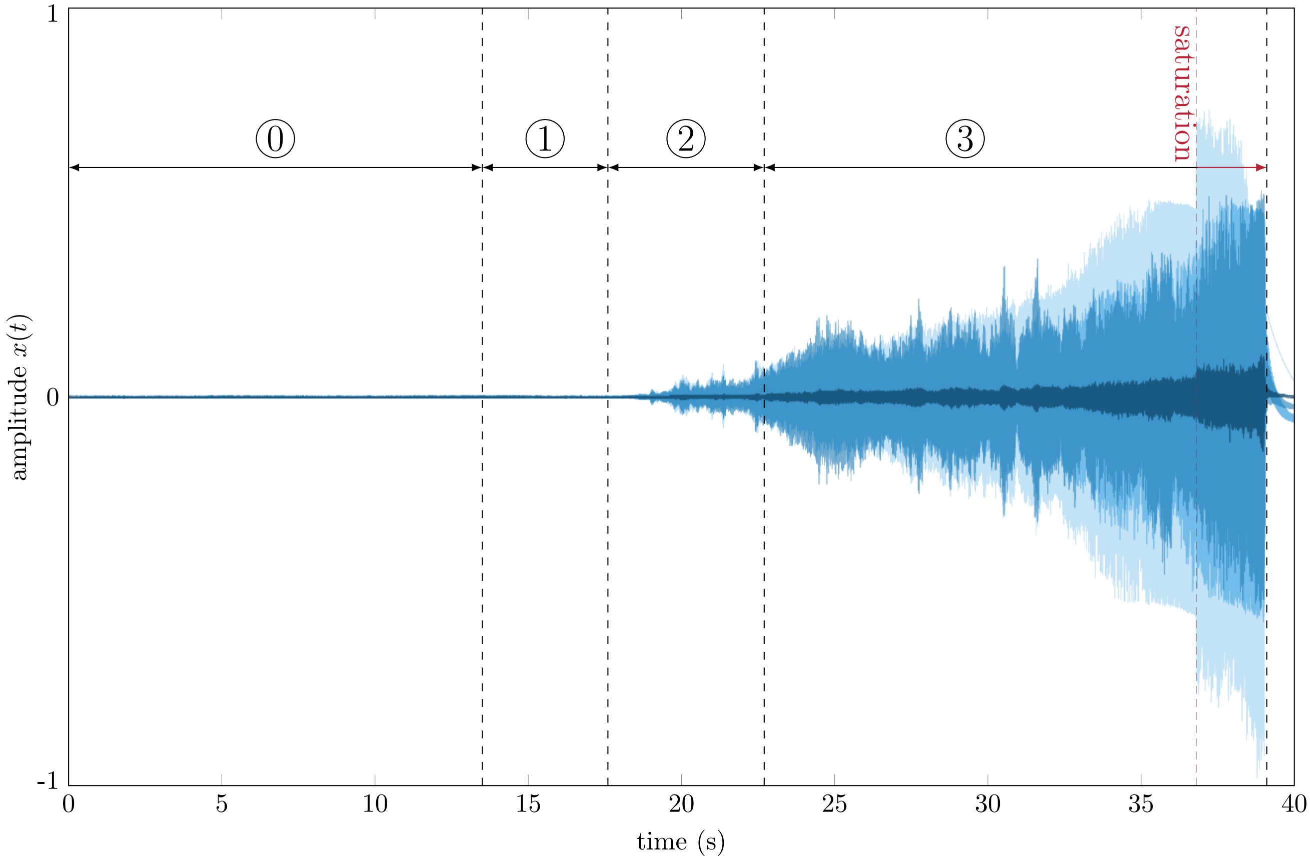

**Figure 5.** Time signals of G1 (—), G2 (—), G3 (—) and G4 (—)

to this instability between an interaction 1B/EO7 and 1B/EO8. The polar representation of the signal during this instability showed patterns with 21 oscillations alternating with patterns comprising 8 oscillations. A portion of the signal, taken at $t = 19$s, exhibiting 21 oscillations has been highlighted (—) in Fig. 7d. At last, during phase 3, frequency of mode 1B synchronizes with EO8's frequency.

### 3.5 Summary of the calibration test

The rotor/stator interaction observed led to blade failure and significant wear of the abradable coating. A synchronization between the blade's first bending mode and EO8 is at the origin of this phenomenon. Quantities of interest extracted from this experiment are summarized in Tab. 1.

## 4 Numerical calibration

Coros is not the only numerical methodology calibrated on this contact scenario involving blade B1. The reader may also refer to a recent publication [11] in which a more versatile numerical code, METAFOR, was used specifically for the simulation of the calibration test.

### 4.1 Numerical strategy

Coros has already been validated using several experimental setups [10], [24], [26]. It is based on an explicit time integration procedure [20]. At each time step, the displacement field of the blade is computed using a central finite difference scheme followed by a correction procedure should penetration in the abradable coating be predicted [27]. Abradable removal and contact treatment rely on a dedicated wear law and the computation of

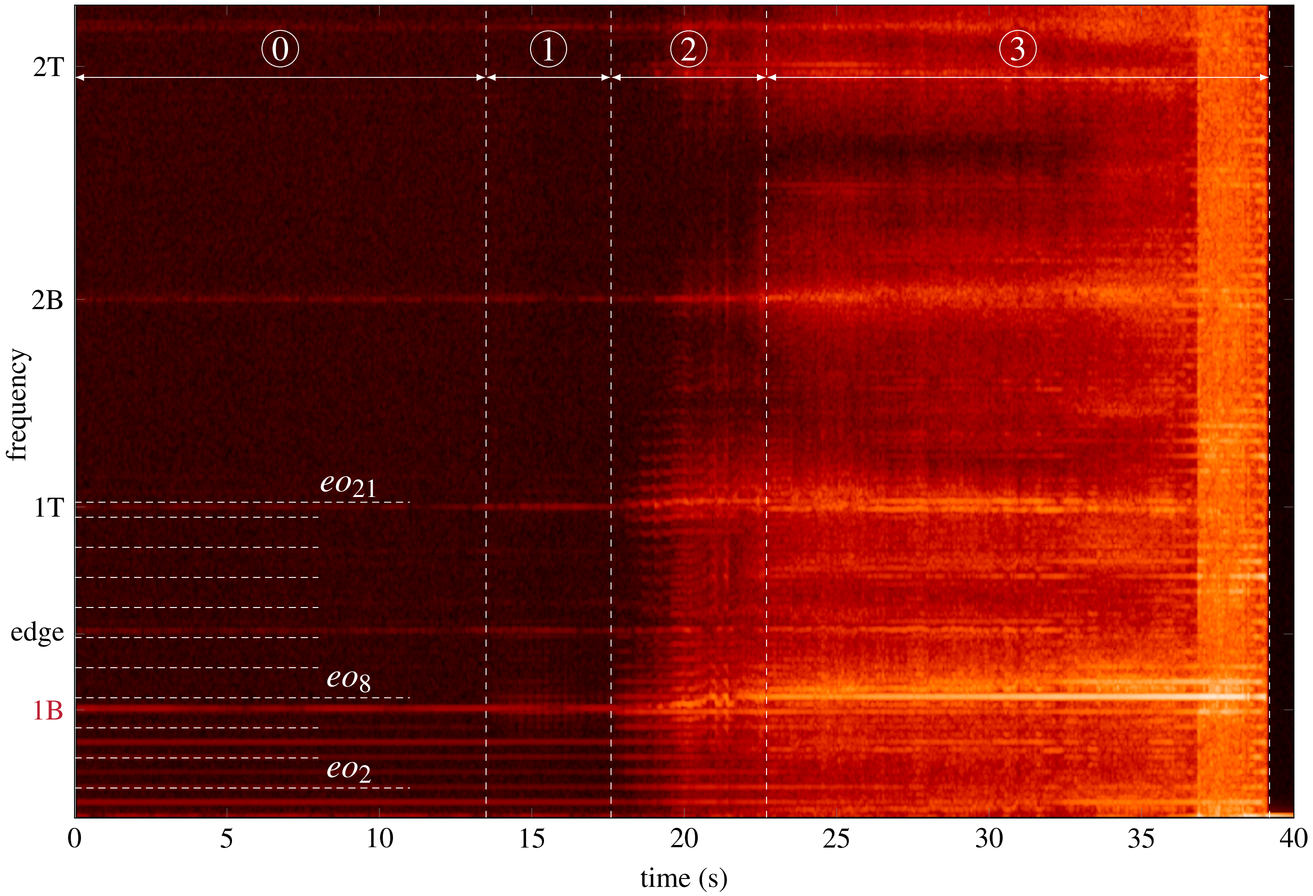

**(a)** Full spectrogram.

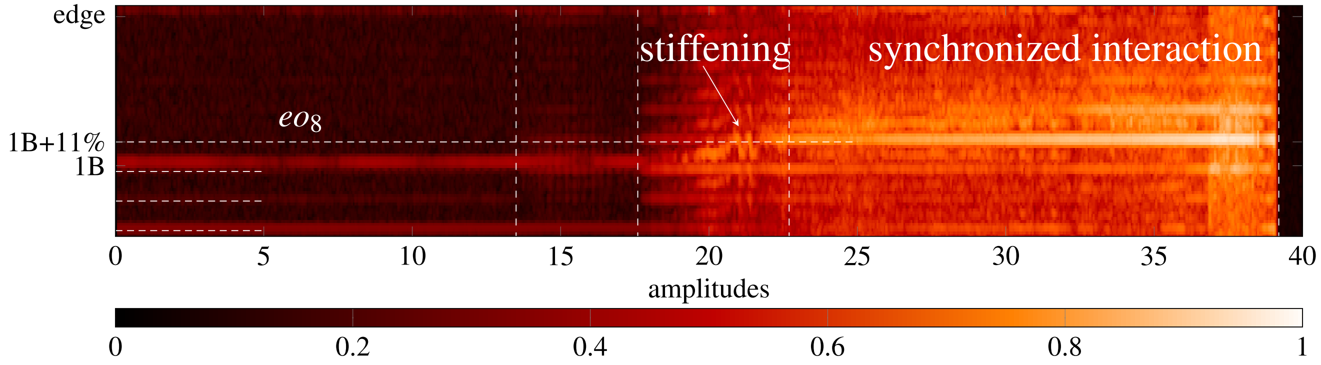

**(b)** Zoom around mode 1B.

**Figure 6.** Spectrogram of the time signal acquired by G1.

Lagrange multipliers [20]. The casing is assumed perfectly rigid, in accordance with experimental observations. The abradable liner is discretized by a succession of one-dimensional rod elements. As of now, the model does not account for realistic mechanical properties of the liner. Necessary parameters—Young's modulus $E$, plastic modulus $K$ and the yield limit $\sigma_y$—are empirical and determined from past calibrations.

Contact is initiated by imposing a progressive ovalization of the casing. The duration of this casing ovalization

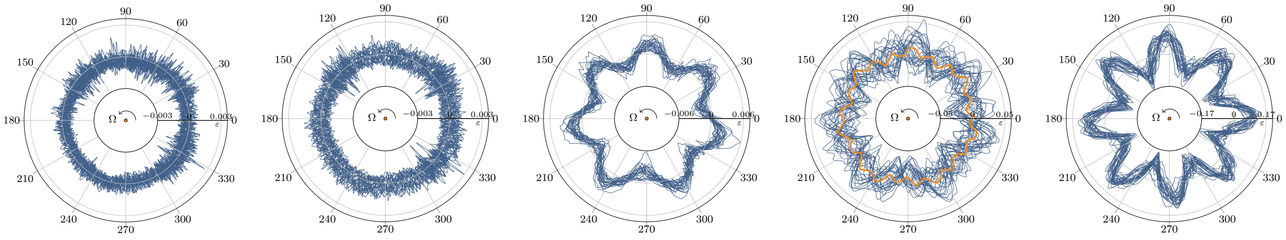

**(a)** Phase 0 **(b)** Phase 1 **(c)** Phase 2a **(d)** Phase 2b **(e)** Phase 3

**Figure 7.** Polar representation of time signal G1 for each identified phases.

**Table 1.** Experimental results of the calibration test

| Results | |
|---|---|
| Type of rotor/stator interaction | Divergent |
| Contact stiffening | 11.5% |
| Critical angular speed | $\Omega_c$ |
| Number of wear lobes / Crossed EO | 8, no angular shift |
| Location of maximum wear | Mid chord, then TE |
| Maximum wear depth [mm] | 0.681 |
| Participating modes | 1B & 1T |

can be adjusted based on the duration of the simulation and the desired contact scenario. Also, the number of deformation lobes and their size can be specified as well. Finally, the current numerical strategy does not account for thermal effects.

### 4.2 Modeling of blade B1

The blade model is composed of 146,150 nodes and 94,289 elements within one body representing the blade and its custom made mount (kept hidden for confidentiality reasons). A fixed restraint, highlighted in orange in Fig. 8, is applied to the face supporting the blade, which is consistent with previous models analyzed with Coros. Nine boundary nodes are selected on the blade tip chord for the contact and wear management. For the sake of computational efficiency, a modal reduction scheme, based on the Craig-Bampton method [28], is employed to reduce the dimension of the numerical model. Degrees of freedom (dof) along the blade-tip/casing interface constitute the boundary nodes retained in the reduced order model. Centrifugal effects are accounted for by interpolating the effects between three stiffness matrices calculated at different speeds $(0, \frac{\Omega}{2}, \Omega)$ [29].

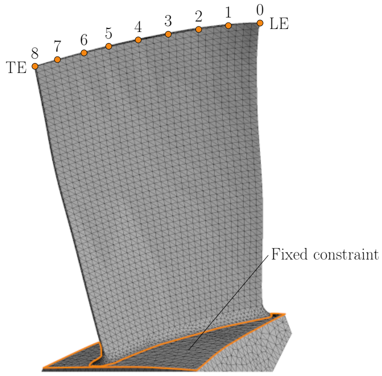

**Figure 8.** Blade model with boundary nodes and fixed constraint.

The reduced-order model is validated through two main steps. Firstly, its first five eigenfrequencies are compared with those of the complete model, showing almost perfect correspondence as soon as $\eta = 10$ fixed-interface modes are retained in the reduction basis. Secondly, the eigenfrequencies of the reduced model are validated against those of the industrial partner's model, revealing a low relative error (+3% or less). Finally, frequencies throughout the considered angular speed range are compared by superimposing both Campbell diagrams. The reduced-order model eigenfrequencies are, in general, slightly stiffer than those of the model used by the industrial partner, mainly due to the fixed constraint. Nevertheless, they are deemed satisfactory to move forward with the simulation of the calibration test.

## 4.3 Calibration of simulation parameters

Multiple parameters are required to numerically define the contact scenario. In order to calibrate the numerical model, each parameter's influence on the results was assessed through sensitivity analyses. Initial tip clearances were calibrated based on the physical configuration of the test bench.

**Initial tip clearances $c$:** Accurate definition of tip clearances at the boundary nodes is essential to replicate the contact scenario. Based on tip clearances measured at rest, numerical tip clearances are computed accounting for centrifugal stiffening for each considered angular speed. It is verified that, in agreement with experimental observations, contact is initiated at the leading edge.

**Casing parameters $t_c$ and $e_p$:** Contact is initiated by the deformation of the casing into two symmetrical lobes diametrically opposed. The contact severity is influenced by two parameters. The first parameter $t_c$ determines the time allocated for the lobe to fully form. A shorter time means that the blade will hit the deformed casing sooner during the simulation. The second parameter, called equivalent penetration $e_p$, represents the depth of the lobe, in millimeters, into the blade's path. The latter directly affects wear levels. These parameters were calibrated to obtain wear levels matching those observed experimentally during the calibration test.

Regarding the mechanical properties of the abradable liner, a very low yield stress $\sigma_Y$ was chosen to favor the wear of the coating. Other parameters, (Young's modulus $E$, plastic modulus $K$ and friction coefficient $\mu$) were empirically selected.

## 4.4 Numerical results

One hundred simulations are run over an angular speed range centered on the experimental critical speed $\Omega_c$. Three-dimensional displacements of the blade at the boundary nodes and wear levels are directly accessible with Coros. All the figures presented in the following have been produced using an original post-processing routine developed in Python.

### 4.4.1 Interaction maps

An interaction map represents the evolution of the steady-state frequency content of displacement signals at specific boundary nodes with respect to the angular speed $\omega$. In practice, these maps are generated by applying a Fast Fourier Transform (FFT) to the radial displacements predicted for each angular speed $\omega$. The establishment of steady-state is checked prior to the computation of the FFT for which only the last 20 revolutions of the simulation are considered. Interaction maps highlight frequencies and angular speeds at which the blade is more likely to respond. Figure 9 illustrates the frequency content of the radial displacements of the blade's TE. The magnitude of the signal is illustrated through a logarithmic color map, ranging from black for lowest amplitudes, to red and then to white for the highest. Frequencies of modes 1B and 1T are marked in red on the y-axis. Speeds are normalized as a function of the interaction speed $\Omega_c$. The interaction map plotted in Fig. 9 underlines the participation of both modes 1B and 1T throughout the angular speed range of interest. Since the experimental interaction is witnessed between mode 1B and EO8, close attention is given to amplitudes along EO8. One can notice that angular speeds between $0.98\Omega_c$ and $1.01\Omega_c$ correspond best to the experimentally observed interaction, due to the high amplitude signals close to the 1B/EO8 crossing.

### 4.4.2 Wear maps and patterns

Wear maps are another useful representation of the vibratory behavior of the blade across a wide range of speeds. They are obtained by stacking the wear levels from the last revolution of each simulation. The $y$ coordinate

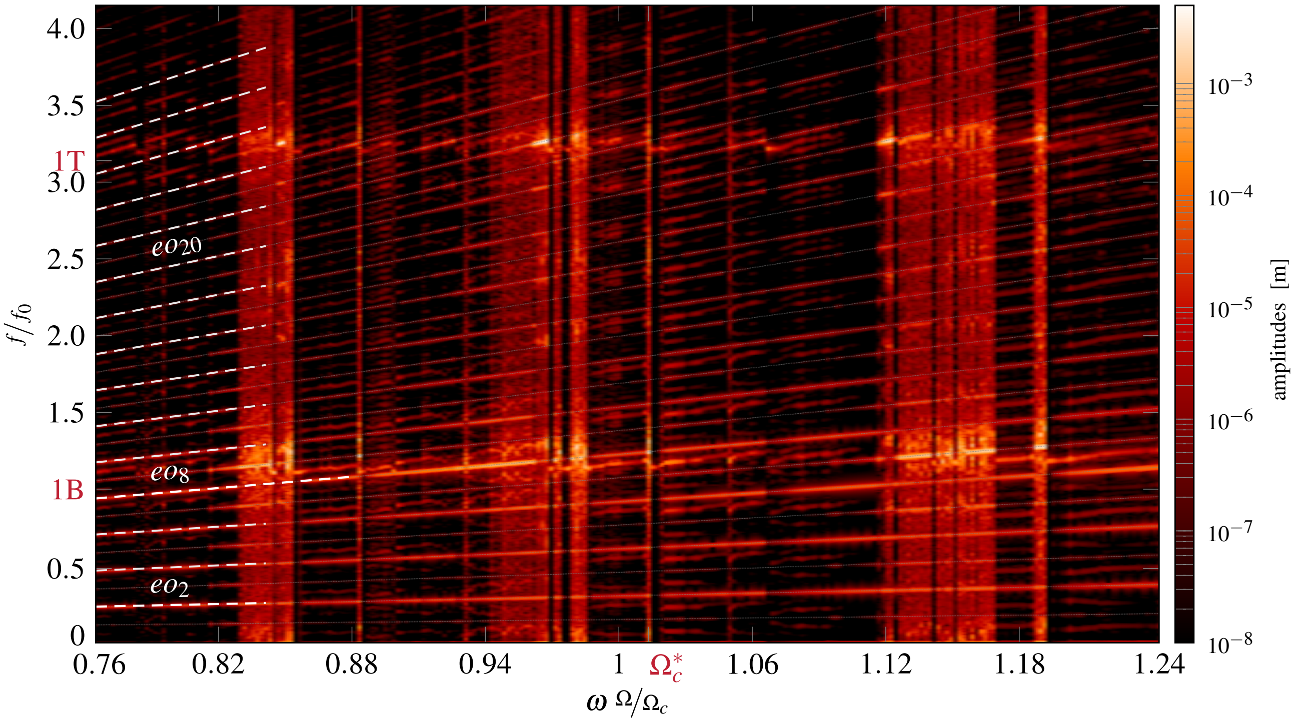

**Figure 9.** Interaction map for the reference blade at the TE.

corresponds to the position along the circumference of the casing, from 0 to 360 degrees. Figure 10 displays the predicted wear profiles at the TE. Deeper wear lobes are indicated by a yellow color (2 mm and over). At speed $1.01\Omega_c$, eight distinct lobes are clearly noticeable. This motivates the choice of $\Omega_c^* = 1.01\Omega_c$ as the numerical critical speed.

After establishing the numerical critical speed, further analyses are conducted to better characterize the predicted rotor/stator interaction. For instance, the time history of wear profiles may be extracted for all the boundary nodes. Figure 11 shows the location of the wear lobes at the LE (11a), middle chord (11b) and TE (11c) in a similar fashion to Fig. 4. Intermediate wear profiles are displayed gradually from white (beginning of the interaction) to black (end of the interaction). The last resulting wear profile, used to generate the wear maps, is highlighted in orange. In Fig. 11b, it is apparent that, over time, the wear lobes grow in the radial direction alone. There is no rotation of the wear lobes over time which indicates a perfect synchronization between mode 1B and EO8 from the beginning of the simulation. Overall, wear patterns are similar to the experimental ones: there is no discernible pattern at the LE while distinct 8-lobe patterns are visible at the middle of chord and TE, with maximum wear at the middle of chord.

### 4.5 Summary of the numerical calibration

Table 2 sums up the results obtained with Coros following its calibration. A divergent rotor/stator interaction of the same nature as the one observed experimentally is predicted at an angular speed near the experimental critical speed. Contact stiffening is assessed by comparing the frequency at which the interaction is observed with the frequency predicted by the Campbell diagram at $\Omega_c^*$. Furthermore, wear patterns at the LE, middle of chord and TE match the experimental observations. However, predicted wear levels are three times greater than the measured wear of 0.681 mm, suggesting that the blade undergoes significant displacements. This raises concerns about the physical meaning of those results and thus motivates the development of a method to discern non physical results in order to obtain relevant wear levels.

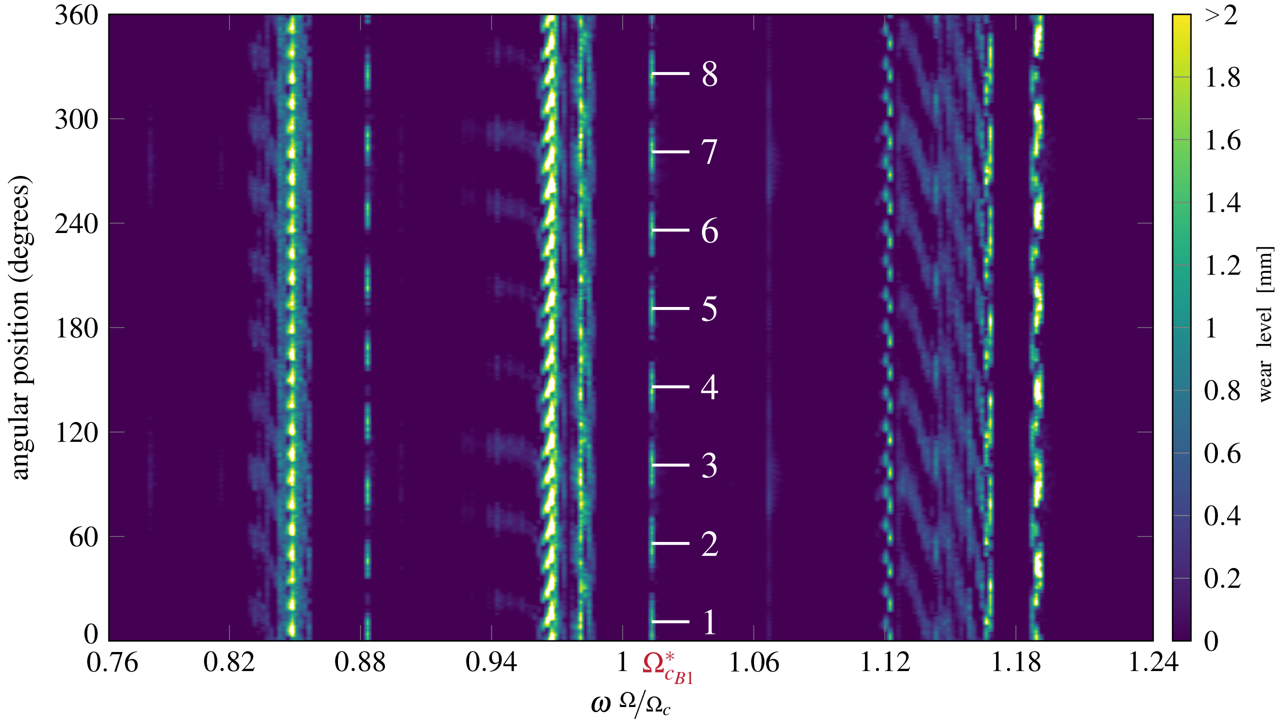

**Figure 10.** Wear maps at the TE. Wear levels are in mm.

**Table 2.** Numerical results of the simulation of the calibration test

| Numerical results | Calibrated simulation |
|---|---|
| Type of rotor/stator interaction | Divergent |
| Contact stiffening | 8.88% |
| Critical angular speed | $\Omega_c^* = 1.01\Omega_c$ |
| Nb of wear lobes / Crossed EO | EO=8, no angular shift |
| Maximum wear depth [mm] | ¿2 |
| Location of maximum wear | Mid chord, then TE |
| Participating modes | 1B & 1T |

## 5 Cut-off criterion

Experimentally, the calibration test stops upon loss of contact, presumably coinciding with blade failure. However, significant displacements in the millimeter range are predicted numerically, which contradicts the hypothesis of small displacements. In order to improve the fidelity of the numerical predictions, it is proposed to consider that stresses within the blade should never exceed its material's yield strength. Accordingly, a cut-off criterion $t_{co}$, corresponding to the instant where this stress is reached, is established. Since this criterion is based solely on local yielding, it is a very simplified view of the complex damage mechanisms at play when the blade undergoes structural contact. Nevertheless, it is expected to provide a conservative estimate of blade failure and therefore represents a first step towards improving the physical relevance of numerical results. In the case of the calibration test, maximal stresses within the blade are predicted close to its root, see Fig. 12. The numerical model predicts that stresses exceeding the blade's yield strength occur as early as $t_{co} = 0.47$ s, see Fig. 13. This corresponds to the 37th blade revolution and explains why previous results featured significantly higher wear levels than those experimentally observed.

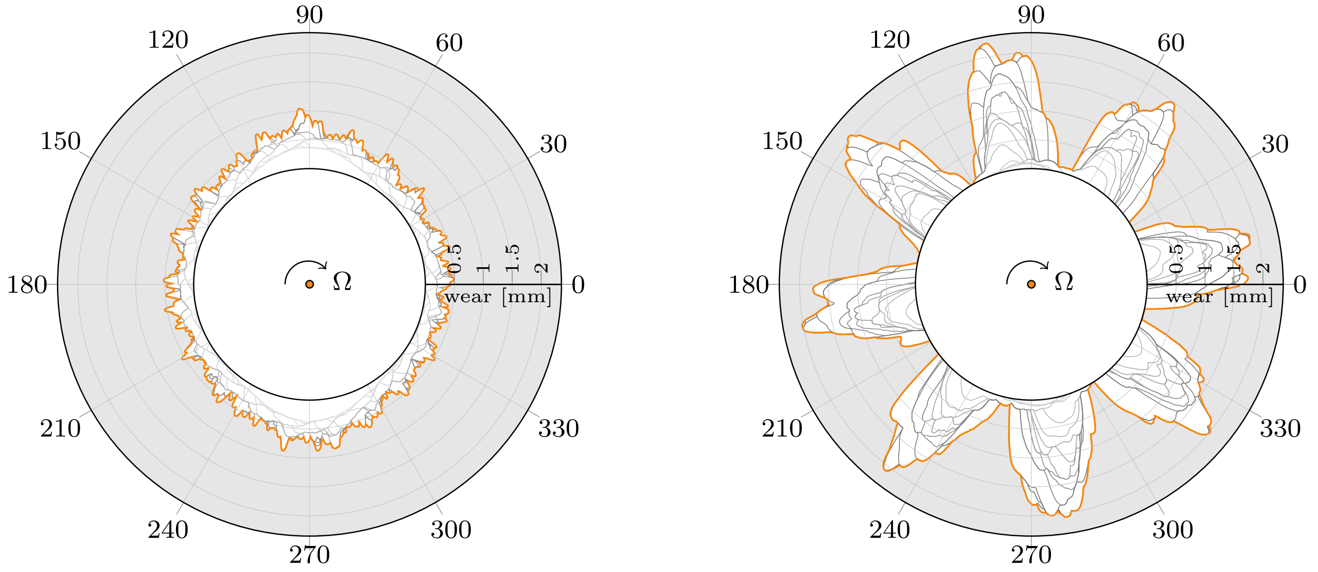

**(a)** LE

**(b)** Mid Chord

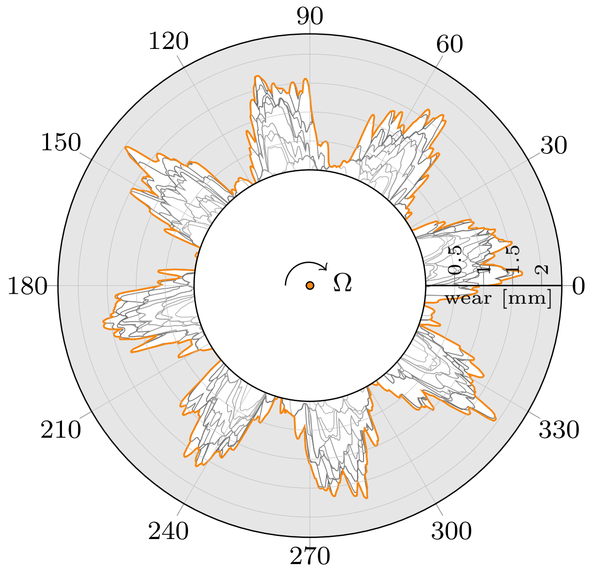

**(c)** TE

**Figure 11.** Progressive wear profiles at $\Omega_c^*$.

However, the way wear is computed implies that there is a delay between the blade vibration and its manifestation in actual wear levels. This lag is directly related to the employed wear model. Though this model advantageously allows for a live update of blade-tip/abradable coating clearances at a negligible computational cost, it has also been found to slightly overestimate the elastic deformation of abradable elements. Conjointly, this leads to an underestimation of plastic deformations which define wear levels. As a result of lower plastic deformation, for a given time step where the blade impacts the coating, its actual penetration within the abradable coating is greater than the coating wear depth predicted by Coros. To mitigate this effect, it is thus necessary to account for wear levels at a further point in time. That is the reason why the cut-off criterion is now defined as $1.25 \times t_{co}$.

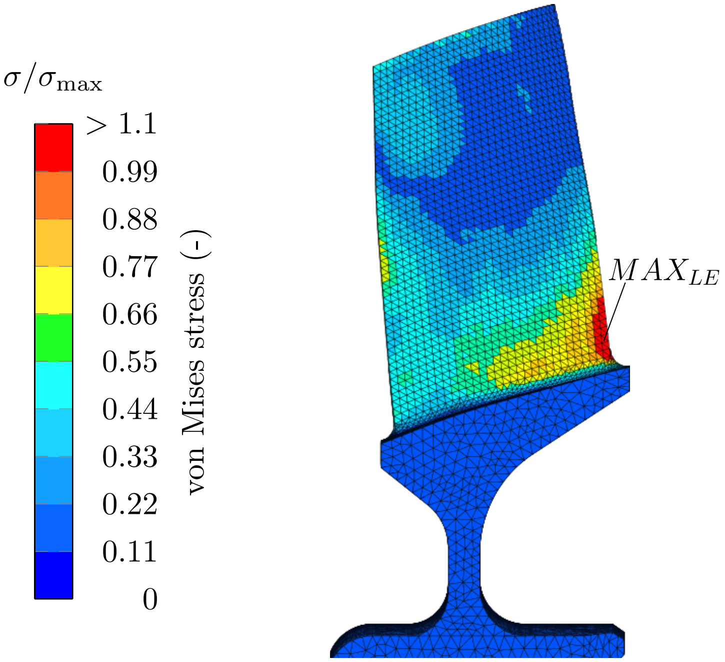

**Figure 12.** Location of the high stresses zone $MAX_{LE}$ (pressure side).

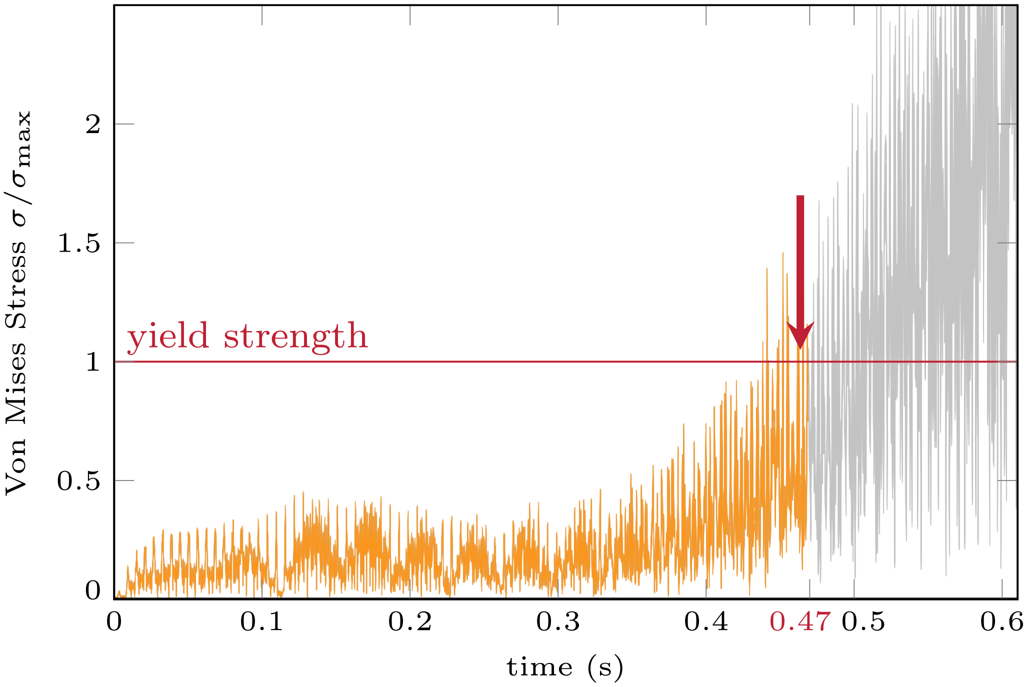

**Figure 13.** Time signal of the Von Mises stresses on zone $MAX_{LE}$.

Per these considerations, wear profiles numerically predicted for the calibration test at the middle of chord ( 14a) and TE ( 14b) are updated, showing in orange the final revolution corresponding to $1.25 \times t_{co}$. Maximum predicted wear levels are around 0.6 mm both at the middle of chord and TE which is very close to experimental observations.

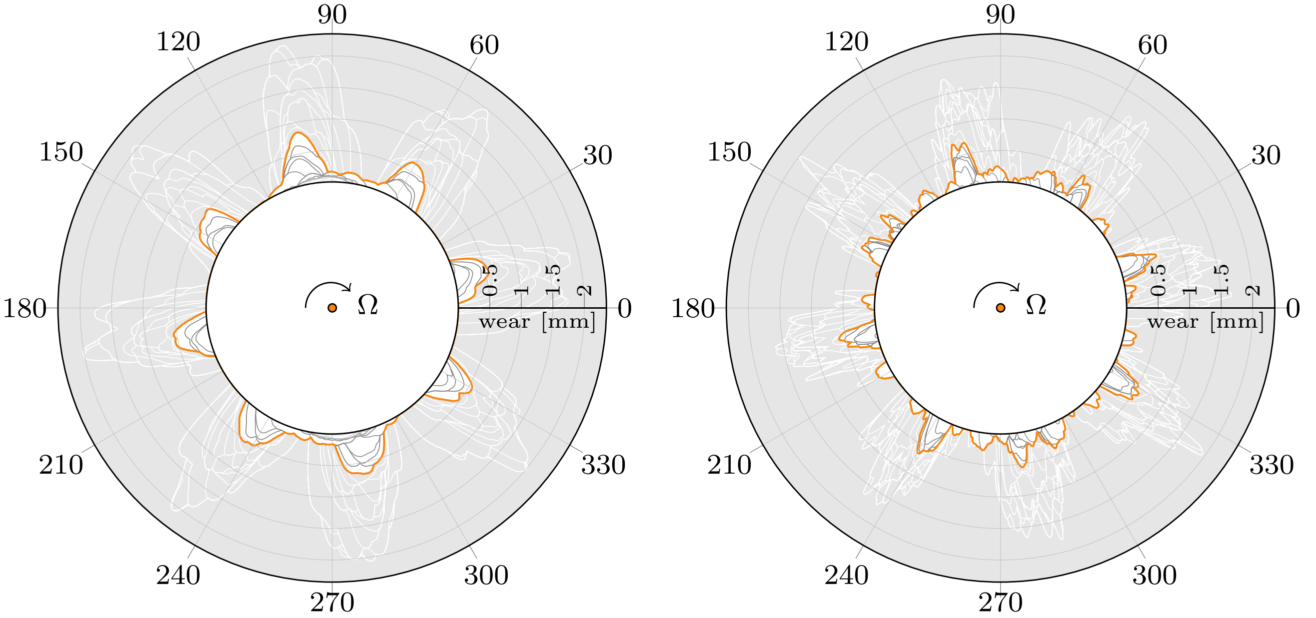

**(a)** Mid chord

**(b)** TE

**Figure 14.** Wear profiles over time at $\Omega_c^*$ until $1.25 \times t_{co}$.

Discarded profiles are shown in white.

## 6 Model validation against tests B2, B3 and B4

Based on the calibration carried out in the previous section, Coros is used with different blade models (B2, B3 and B4) to simulate the other contact interactions numerically. For each blade model, a finite element model is built and validated using the same procedure as described in 4.2. In this section, subsequent tests are described briefly. Experimental and numerical results are also presented. The results are summarized at the end of the section in Tab. 3 for easier comparison. Experimental speed of interaction, $\Omega_c$ always refers to the current blade test.

### 6.1 Simulation of test B2

B2 is a compressor blade, more elongated and less twisted than B1. Two contact tests at different angular speeds have been conducted on B2, and only the last one showed a brief synchronization at speed $\Omega_{c_{B2}}$. No damage was observed on the blade and low wear levels were measured on the abradable. Frequency content of the strain gauges signals exhibited a high amplitude peak along B2's first bending mode, hesitating between a synchronization with EO7 and EO8. Ultimately, the interaction happened between the first bending mode and the eighth engine order (1B/EO8).

Low wear levels measured on the abradable at the LE and middle of chord did not show any clear pattern. At these locations, the abradable was worn all around its circumference. At the TE, 8 large wear lobes can be observed. An imperfect synchronization between the vibration of the blade and the angular speed of the engine during the major duration of the test could be responsible for the circumferential shift of the wear lobes, leading to larger lobes and, eventually, constant wear levels.

With the set of calibrated parameters, Coros is used to simulate contact scenarios on a large range of angular speeds neighboring the interaction speed $\Omega_{c_{B2}}$. Figure 15a shows the interaction map generated from the radial displacements at the TE of blade B2. Zones of high amplitudes are restrained on fewer angular speeds; around 0.95, 1.12 and $[1.27 - 1.39]\Omega_{c_{B2}}$. At those engine speeds, the blade's first bending mode answers on engine orders from 6 to 8.

Resulting wear profiles at the TE predicted after 100 revolutions are illustrated on Fig. 15b. Only few angular speeds, typically showing high amplitudes on the interaction map, lead to significant wear, demonstrating the low sensitivity of B2 to contact. The numerical critical speed is identified as $\Omega^*_{c_{B2}} = 0.94\Omega_c$, where 8 wear lobes are visible.

Progressive wear profiles at the critical speed were plotted taking into account the cut-off criterion. Abradable is expected to be worn in 8 positions at the LE and TE. Maximum wear levels predicted by Coros are superior (0.8 mm) than the experimental measurements (0.21 mm) despite the $t_{co}$. This probably results from the choice of critical speed. An angular speed leading to a divergent rotor/stator interaction was deliberately chosen. Experimentally, however, no damage was observed on B2. This is because the interaction stabilised itself before the appearance of large displacements.

### 6.2 Simulation of test B3

B3 shares a geometry similar to B1. One contact experiment was conducted on blade B3 resulting in the blade cracking at its root. The cause of the blade's rupture was the synchronization between mode 1B and the EO8, as indicated by the analysis of the frequency content of the strain gauge signals. A wear pattern with 8 lobes was observed in front of the middle of chord. The frequency analysis of the strain gauges signals highlighted the first bending mode as the main contributing mode to this interaction. The second bending mode was also a contributing factor, albeit in lesser proportion.

Maximum wear (0.435 mm) is located in front of the middle of chord. At the TE, where the tip clearances are the largest, the abradable liner remained almost intact. At the LE, wear levels were in general lower than the middle of chord (0.2 mm) and the wear pattern was less defined.

From the interaction map in Fig. 15c, the interaction sought is between speeds $[0.90;0.94]\Omega_{c_{B3}}$, where the EO8 is crossing the first bending mode frequencies. At these angular speeds, the interaction map underlines the participation of modes 1T and 2B.

Wear levels at the TE remain consistently low across the analyzed speed range, except for the critical speed identified as $\Omega_{c^*_{B3}} = 0.94\Omega_{c_{B3}}$. At the LE, not included here, wear levels are even lower. Based on this observation, B3 appears to be more robust in handling repetitive contact compared to its counterpart B1 (see Fig. 10).

### 6.3 Simulation of test B4

B4 is the last blade studied as part of this test campaign. B4 presents significant differences in terms of geometry and operating conditions compared to the other blades discussed in this paper (B1 to B3). Specifically, it is shorter, more twisted, and operates at angular speeds 1.5 times higher than the interaction speed of B1. The numerical simulation of the contact scenario involving B4 serves as the limit case for this validation. During the experiment, severe damage occurred. B4's blade tip at its leading edge was completely torn off, demonstrating its high sensitivity to contact. Wear profiles at the TE revealed seven perfectly radial wear lobes, each approximately 0.6 mm deep. Maximum wear depth reached 0.759 mm also at the TE. At the LE and middle of chord, wear levels were less important, respectively 0.2 mm and 0.4 mm. Frequency analysis of the radial displacements concluded that the first bending mode of B4 synchronized with the frequency of EO7, leading to a divergent contact interaction. Given the extreme temperatures nearing 1600°C at the blade tip, reproducing this experiment with the calibrated parameters represents the limit case since thermo-mechanical effects are neglected in the current numerical strategy.

The same methodology was applied to generate a FEM model of B4. However, within all the blade models, this one showed the largest variation on its eigenfrequencies with the industrial partner's model. An overestimation of 6.6% on the first bending mode frequency was calculated. While not critical, this difference will have an impact on the prediction of the numerical critical speed. Interactions map at the TE (see Fig. 15e) indicates an interaction with EO8 (from $0.88\Omega_{c_{B4}}$ to $0.93\Omega_{c_{B4}}$) and an interaction with EO7 (from $1.05\Omega_{c_{B4}}$ onward). Notably, Coros predicted a rotor/stator interaction accompanied with high amplitude vibrations over a broad range of angular speeds. This suggests that B4 is easily synchronized with an engine order and highly sensitive to contact. Wear map on Fig. 15f shows large sections where the abradable liner is completely removed. Similar 7 wear lobes pattern is obtained at the TE. Numerical critical speed was chosen on the left side of the critical speeds range, at $\Omega_{c^*_{B4}}$=$1.06\Omega_{c_{B4}}$. Predicted wear profiles at the numerical critical speed showed major differences with the experimental results.

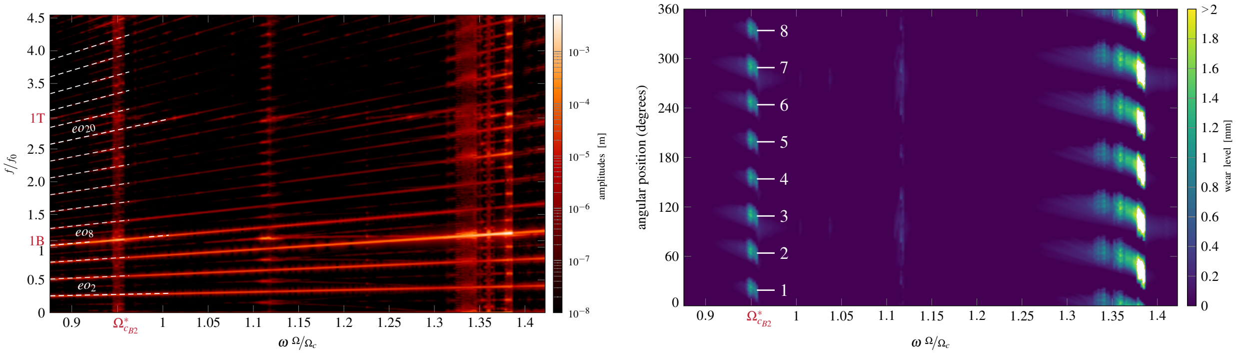

**(a)** Interaction map at the TE for blade B2.

**(b)** Wear map at the TE for blade B2.

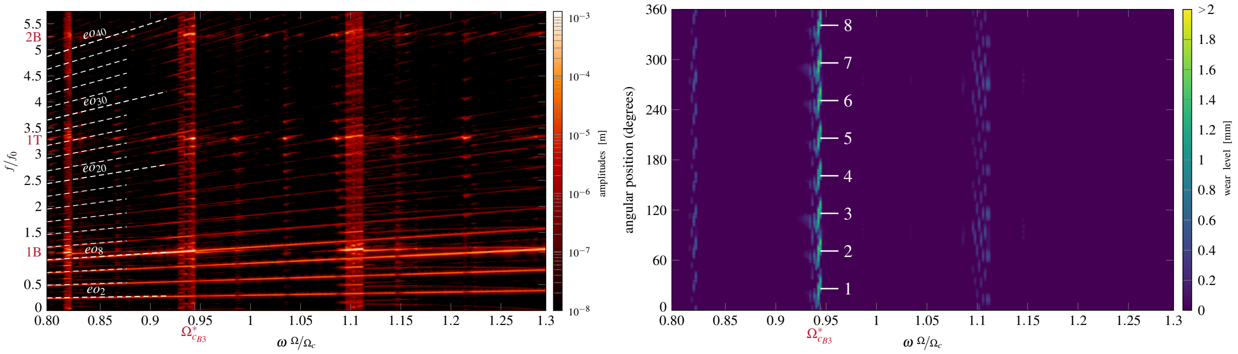

**(c)** Interaction map at the TE for blade B3.

**(d)** Wear map at the TE for blade B3.

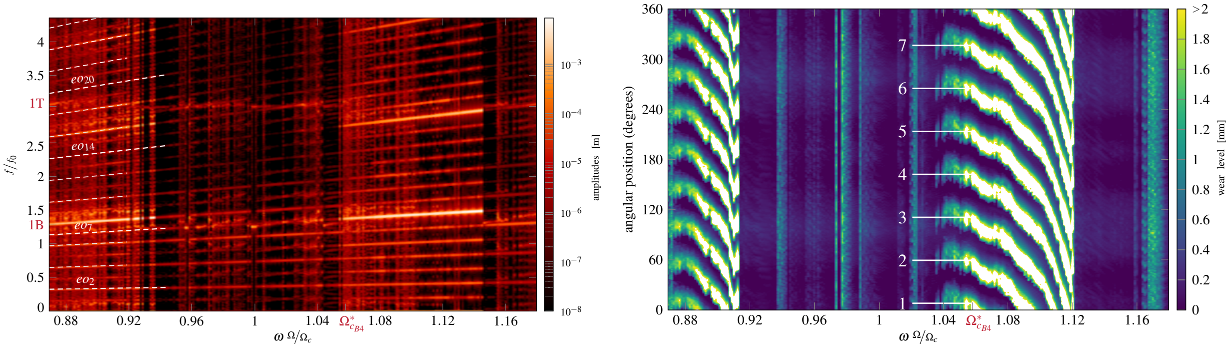

**(e)** Interaction map at the TE for blade B4.

**(f)** Wear map at the TE for blade B4.

**Figure 15.** Interaction maps and predicted wear plevels for blades B2, B3 and B4.

Indeed, maximum wear was predicted at the LE, while, experimentally, high wear levels were located in front of the TE followed by the mid-chord.

### 6.4 Summary of blind numerical simulations

Comparison between experimental data and numerical results are presented in Tab. 3.

These results highlight that the numerical calibration of Coros for blade B1 solely allowed to blindly simulate numerical interactions experimentally observed on blade B2, B3, and B4 with good accuracy. In particular, the numerical strategy accurately predicts divergent interactions in the vicinity of the experimental critical angular speed.

Contrary to previous validation studies that were more limited in scope, it is possible here to observe that the

**Table 3.** Comparison between numerical and experimental results for blades B2, B3 and B4.

| Results | Blade B2 | | Blade B3 | | Blade B4 | |
|---|---|---|---|---|---|---|
| | Exp | Numerical | Exp | Numerical | Exp | Numerical |
| Type of interaction | steady | divergent | divergent | divergent | divergent | divergent |
| Contact stiffening | 9.8% | 1.7% | 11.8% | 2.9% | 6.5% | 7.6% |
| Critical angular speed | $\Omega_{c_{B2}}$ | $0.95\Omega_{c_{B2}}$ | $\Omega_{c_{B3}}$ | $0.94\Omega_{c_{B3}}$ | $\Omega_{c_{B4}}$ | $1.06\Omega_{c_{B4}}$ |
| Number of wear lobes / Crossed EO | 8 | 8 | 8 | 8 | 7 | 7 |
| Location of maximum wear | TE | LE | Mid | TE | TE | LE |
| Maximum wear depth [mm] | 0.216 | 0.8 | 0.435 | 0.5 | 0.759 | $\approx 2$ |
| Participating modes | 1B & 1T | 1B | 1B & 2B | 1B, 1T & 2B | 1B, 1T & 2B | 1B & 1T |

numerical strategy accurately portrays the relative sensitivity of a blade to structural contacts. Expectedly, blade B4—for which experimental observations clearly showed an exacerbated sensitivity to contact—is predicted as the most sensitive blade. Il is also the most likely to undergo very high amplitudes of vibration alongside extreme wear levels of the abradable coating. On the other hand, blade B2—for which the experimental synchronization on a critical speed was arduous and practically no wear of the coating was measured—does not feature significant amplitudes of vibration from a numerical standpoint. These results thus confirm that the proposed numerical strategy could be utilized to discriminate blade profiles with respect to their sensitivity to structural contacts.

## 7 Conclusion

This paper presents the calibration and validation of a specialized numerical tool designed for predicting blade-tip/casing contact interactions in aircraft engines. From an extensive experimental campaign dedicated to such interactions, an existing numerical strategy is first calibrated using experimental data specific to a particular blade. Owing to the addition of a cut-off criterion designed to ensure that numerical results remain physically relevant, it is shown that the current numerical strategy provides very accurate predictions in terms of critical angular speed and stress levels. Concerning the abradable coating wear levels, the application of the cut-off criterion constitutes a first step towards more accurate wear predictions. As expected, and despite its simplicity, this cut-off criterion allows to significantly increase the physical relevance of the predicted results. Future work could focus on improving its definition to be more representative of the blade failure mechanisms. Building on this calibration, the numerical strategy is then run blindly using other blade models in order to assess its versatility. Overall, a very good agreement is found between numerical predictions and experimental data for each blade considered. More importantly, the relative sensitivity of each blade to structural contacts is accurately predicted, which demonstrate that the numerical strategy could be used for the discrimination of blades too sensitive to contact interactions.

## Acknowledgments

This work was made possible thanks to the valuable collaboration and financial support of Safran Aero Boosters (Belgium) and the participation of Safran Aircraft Engines in the development of Coros.

## References

[1] Ma, H., Yin, F., Guo, Y., Tai, X. and Wen, B. "A review on dynamic characteristics of blade–casing rubbing." *Nonlinear Dynamics* Vol. 84 No. 2 (2015): pp. 437–472. DOI 10.1007/s11071-015-2535-x.

[2] Agrapart, Q., Nyssen, F., Lavazec, D., Dufrénoy, P. and Batailly, A. "Multi-physics numerical simulation of an experimentally predicted rubbing event in aircraft engines." *Journal of Sound and Vibration* Vol. 460 (2019). DOI 10.1016/j.jsv.2019.114869.

[3] Delebarre, C., Wagner, V., Paris, J.-Y., Dessein, G., Denape, J. and Gurt-Santanach, J. "Tribological characterization of a labyrinth-abradable interaction in a turbo engine application." *Wear* Vol. 370-371 (2017): pp. 29–38. DOI 10.1016/j.wear.2016.11.007.

[4] Michael, W. and Matthew, M. "Wear mechanisms at the blade tip seal interface." *Wear* Vol. 404-405 (2018): pp. 176–193. DOI https://doi.org/10.1016/j.wear.2018.03.009.

[5] Mandard, R., Witz, J.-F., Boidin, X., Fabis, J., Desplanques, Y. and Meriaux, J. "Interacting force estimation during blade/seal rubs." *Tribology International* Vol. 82 (2015): pp. 504–513. DOI 10.1016/j.triboint.2014.01.026.

[6] Tang, N., Zhang, B., Lord, C. and Marshall, M. "Identification of blade operational mode shapes during wear of abradable coating." *Journal of Sound and Vibration* Vol. 472 (2020): p. 115204. DOI 10.1016/j.jsv.2020.115204.

[7] Zhang, B. and Marshall, M. "Investigating material removal mechanism of Al-Si base abradable coating in labyrinth seal system." *Wear* Vol. 426-427 (2019): pp. 239–249. DOI 10.1016/j.wear.2019.01.034.

[8] Delebarre, C., Wagner, V., Paris, J. Y., Dessein, G., Denape, J. and Gurt-Santanach, J. "An experimental study of the high speed interaction between a labyrinth seal and an abradable coating in a turbo-engine application." *Wear* Vol. 316 No. 1 (2014): pp. 109–118. DOI 10.1016/j.wear.2014.04.023.

[9] Millecamps, A., Brunel, J.-F., Dufrenoy, P., Garcin, F. and Nucci, M. "Influence of Thermal Effects During Blade-Casing Contact Experiments.": pp. 855–862. 2010. American Society of Mechanical Engineers Digital Collection. DOI 10.1115/DETC2009-86842.

[10] Batailly, A., Legrand, M., Millecamps, A. and Garcin, F. "Numerical-experimental comparison in the simulation of rotor/stator interaction through blade-tip/abradable coating contact." *Journal of Engineering for Gas Turbines and Power* Vol. 134 No. 8 (2012). DOI 10.1115/1.4006446.

[11] Pacyna, L., Bertret, A., Derclaye, A., Papeleux, L. and Ponthot, J.-P. "Implementation of a Rig Test for Rotor/Stator Interaction of Low-Pressure Compressor Blades and Comparison of Experimental Results With Numerical Model." Vol. Volume 11: Structures and Dynamics: Structural Mechanics, Vibration, and Damping; Supercritical CO2 (2020): p. V011T30A006. DOI 10.1115/GT2020-14266.

[12] Lesaffre, N., Sinou, J. J. and Thouverez, F. "Contact analysis of a flexible bladed-rotor." *European Journal of Mechanics - A/Solids* Vol. 26 No. 3 (2007): pp. 541–557. DOI 10.1016/j.euromechsol.2006.11.002.

[13] Legrand, M., Pierre, C., Cartraud, P. and Lombard, J.-P. "Two-dimensional modeling of an aircraft engine structural bladed disk-casing modal interaction." *Journal of Sound and Vibration* Vol. 319 No. 1-2 (2009): pp. 366–391. DOI 10.1016/j.jsv.2008.06.019.

[14] Legrand, M., Batailly, A., Magnain, B., Cartraud, P. and Pierre, C. "Full three-dimensional investigation of structural contact interactions in turbomachines." *Journal of Sound and Vibration* Vol. 331 No. 11 (2012): pp. 2578–2601. DOI 10.1016/j.jsv.2012.01.017.

[15] Legrand, M. and Pierre, C. "Numerical Investigation of Abradable Coating Wear Through Plastic Constitutive Law: Application to Aircraft Engines.": pp. 907–916. 2010. American Society of Mechanical Engineers Digital Collection. DOI 10.1115/DETC2009-87669.

[16] Williams, Robin J. "Simulation of Blade Casing Interaction Phenomena in Gas Turbines Resulting From Heavy Tip Rubs Using an Implicit Time Marching Method.": pp. 1007–1016. 2012. American Society of Mechanical Engineers Digital Collection. DOI 10.1115/GT2011-45495.

[17] Nyssen, F. and Batailly, A. "Sensitivity Analysis of Rotor/Stator Interactions Accounting for Wear and Thermal Effects within Low- and High-Pressure Compressor Stages." *Coatings* Vol. 10 No. 1 (2020). DOI 10.3390/coatings10010074.

[18] Nyssen, F., Colaïtis, Y. and Batailly, A. "Numerical investigation of a mistuned industrial bladed disk dynamics with structural contacts using time and frequency methods." *Journal of Sound and Vibration* Vol. 535 (2022): p. 117077. DOI 10.1016/j.jsv.2022.117077.

[19] Delhez, E., Nyssen, F., Golinval, J.-C. and Batailly, A. “Assessment of Geometric Nonlinearities Influence On NASA Rotor 37 Response to Blade Tip/Casing Rubbing Events.” *Journal of Engineering for Gas Turbines and Power* (2021)DOI 10.1115/1.4051968.

[20] Carpenter, Nicholas J., Taylor, Robert L. and Katona, Michael G. “Lagrange constraints for transient finite element surface contact.” *International Journal for Numerical Methods in Engineering* Vol. 32 No. 1 (1991): pp. 103–128. DOI https://doi.org/10.1002/nme.1620320107.

[21] Colaïtis, Y. “Stratégie numérique pour l’analyse qualitative des interactions aube/carter.” Theses, École Polytechnique de Montréal. 2021.

[22] Vadcard, T., Thouverez, F. and Batailly, A. “On the detection of nonlinear normal mode-related isolated branches of periodic solutions for high-dimensional nonlinear mechanical systems with frictionless contact interfaces.” *Computer Methods in Applied Mechanics and Engineering* Vol. 419 (2024): p. 116641. DOI 10.1016/j.cma.2023.116641.

[23] Nitschke, S., Wollmann, T., Ebert, C., Behnisch, T., Langkamp, A., Lang, T., Johann, E. and Gude, M. “An advanced experimental method and test rig concept for investigating the dynamic blade-tip/casing interactions under engine-like mechanical conditions.” *Wear* Vol. 422-423 (2019): pp. 161–166. DOI 10.1016/j.wear.2018.12.072.

[24] Batailly, A., Agrapart, Q., Millecamps, A. and Brunel, J.-F. “Experimental and numerical simulation of a rotor/stator interaction event localized on a single blade within an industrial high-pressure compressor.” *Journal of Sound and Vibration* Vol. 375 (2016): pp. 308–331. DOI 10.1016/j.jsv.2016.03.016.

[25] Millecamps, A., Batailly, A., Legrand, M. and Garcin, F. “Snecma’s Viewpoint on the Numerical and Experimental Simulation of Blade-Tip/Casing Unilateral Contacts.” *ASME Turbo Expo Conference*. 2015. ASME, Montréal, Canada. DOI 10.1115/GT2015-42682.

[26] Nyssen, F., Tableau, N., Lavazec, D. and Batailly, A. “Experimental and numerical characterization of a ceramic matrix composite shroud segment under impact loading.” *Journal of Sound and Vibration* Vol. 467 (2020). DOI 10.1016/j.jsv.2019.115040.

[27] Legrand, M., Batailly, A. and Pierre, C. “Numerical Investigation of Abradable Coating Removal in Aircraft Engines Through Plastic Constitutive Law.” *Journal of Computational and Nonlinear Dynamics* Vol. 7 No. 1 (2011): p. 011010. DOI 10.1115/1.4004951.

[28] Craig, R. R. and Bampton, M. C. C. “Coupling of Substructures for Dynamic Analyses.” *AIAA Journal* Vol. 6 No. 7 (1968): pp. 1313–1319. DOI 10.2514/3.4741.

[29] Sternchüss, A. and Balmès, E. “On the reduction of quasi-cyclic disks with variable rotation speeds.” *Proceedings of the International Conference on Advanced Acoustics and Vibration Engineering (ISMA)* (2006): pp. 3925–3939.